

See discussions, stats, and author profiles for this publication at: <http://www.researchgate.net/publication/226801102>

High-Throughput Prostate Cancer Gland Detection, Segmentation, and Classification from Digitized Needle Core Biopsies

CHAPTER · JANUARY 1970

DOI: 10.1007/978-3-642-15989-3_10

CITATION

1

6 AUTHORS, INCLUDING:



[Rachel Sparks](#)

University College London

20 PUBLICATIONS 41 CITATIONS

SEE PROFILE



[Andrew Janowczyk](#)

Indian Institute of Technology Bombay

9 PUBLICATIONS 42 CITATIONS

SEE PROFILE



[Michael D Feldman](#)

University of Pennsylvania

197 PUBLICATIONS 4,189 CITATIONS

SEE PROFILE



[Anant Madabhushi](#)

Case Western Reserve University

250 PUBLICATIONS 2,813 CITATIONS

SEE PROFILE

High-Throughput Prostate Cancer Gland Detection, Segmentation, and Classification from Digitized Needle Core Biopsies

Jun Xu¹, Rachel Sparks¹, Andrew Janowczyk^{1,3}, John E. Tomaszewski²,
Michael D. Feldman², and Anant Madabhushi¹

¹ Department of Biomedical Engineering, Rutgers University, USA

² The Hospital of the University of Pennsylvania, Anatomic and Surgical Pathology Informatics, Philadelphia, USA

³ Department of Computer Science and Engineering, Indian Institute of Technology (IIT) Bombay, Mumbai, India

Abstract. We present a high-throughput computer-aided system for the segmentation and classification of glands in high resolution digitized images of needle core biopsy samples of the prostate. It will allow for rapid and accurate identification of suspicious regions on these samples. The system includes the following three modules: 1) a hierarchical frequency weighted mean shift normalized cut (HNCut) for initial detection of glands; 2) a geodesic active contour (GAC) model for gland segmentation; and 3) a diffeomorphic based similarity (DBS) feature extraction for classification of glands as benign or cancerous. HNCut is a minimally supervised color based detection scheme that combines the frequency weighted mean shift and normalized cuts algorithms to detect the lumen region of candidate glands. A GAC model, initialized using the results of HNCut, uses a color gradient based edge detection function for accurate gland segmentation. Lastly, DBS features are a set of morphometric features derived from the nonlinear dimensionality reduction of a dissimilarity metric between shape models. The system integrates these modules to enable the rapid detection, segmentation, and classification of glands on prostate biopsy images. Across 23 H & E stained prostate studies of whole-slides, 105 regions of interests (ROIs) were selected for the evaluation of segmentation and classification. The segmentation results were evaluated on 10 ROIs and compared to manual segmentation in terms of mean distance (2.6 ± 0.2 pixels), overlap ($62 \pm 0.07\%$), sensitivity ($85 \pm 0.01\%$), specificity ($94 \pm 0.003\%$) and positive predictive value ($68 \pm 0.08\%$). Over 105 ROIs, the classification accuracy for glands automatically segmented was ($82.5 \pm 9.10\%$) while the accuracy for glands manually segmented was ($82.89 \pm 3.97\%$); no statistically significant differences were identified between the classification results.

Keywords: High-throughput, geodesic active contour model, morphological feature, prostate cancer, glands, needle biopsy, digital pathology.

1 Introduction

Digital pathology is a rapidly expanding field for the analysis, viewing, and storage of histology tissue samples due to the advent and cost-effectiveness of whole-slide digital scanners [1]. In the context of prostate cancer (CaP), pathologists grade histopathological specimens by visually characterizing gland morphology and architecture in regions they suspect are malignant. The Gleason grading system is used to describe CaP aggressiveness; nonaggressive glands (grade 1) are medium-sized with round shapes, while aggressive glands (grade 5) are small and have irregular shapes [2]. CaP grading of histopathology can therefore be divided into two separate tasks: identification of malignant regions and the Gleason grading of the malignant regions. The ability to quickly and accurately identify suspicious regions in tissue samples will enable the pathologist to focus their grading efforts on candidate regions, minimizing the time spent on identifying CaP regions. Doyle *et al.* [3] have demonstrated the effectiveness for discriminating malignant regions using texture based features at low image resolutions. Recently, Monaco *et al.* [4] showed that gland size can be used to discriminate between malignant and benign glands on high resolution whole mount histopathology of the prostate. Automated schemes for Gleason grading of suspicious regions on prostate histopathology have attempted to leverage gland morphology by quantifying contour variability, length-to-width ratio, or related features [5], [6]. We have recently demonstrated that Diffeomorphic Based Similarity (DBS) features are better able to capture subtle morphometric differences between prostate glands of different Gleason grades than previously reported morphological features [7].

An important pre-requisite to extracting morphological features is the ability to accurately and efficiently detect the location of glands and segment them accurately while preserving important morphological information. While active contour models are good candidate for this task, most active contour models are not able to efficiently handle very large images. Region-based active contour models do not require accurate contour initialization, however they may involve significant computational overhead [8]. Hence, there is a need for rapid identification of the regions of interest in order to initialize the active contour model. Hierarchical mean shift normalized cuts (HNCut) was shown to efficiently determine the location of the region of interest on very large histopathology images [9]. Additionally, for most boundary based active contour models, the evolution function is dependent on the gray scale intensity gradient [10]. We employ a local structure tensor based color gradient, obtained by calculating the local min/max variations contributed from each color channel (e.g. R, G, B or H, S, V), resulting in stronger object boundaries compared to the gray scale gradient.

We present a system which applies a geodesic active contour (GAC) model in conjunction with DBS feature extraction to effectively segment and classify the glandular regions of needle core biopsies of the prostate in a high-throughput manner. Figure 1 shows the flowchart of our system which is comprised of three modules. Module 1 identifies glands using HNCut, an accurate, efficient, and minimally interactive model initialization scheme HNCut. In module 2, our GAC model

initialized by HNCut finds the gland boundaries utilizing a color gradient based edge-detector function. In module 3, DBS features are obtained by computing differences between medial axis shape models of glands, followed by nonlinear dimensionality reduction (Graph Embedding [11]) to extract relevant morphometric features. DBS features are used to train a SVM classifier for distinguishing between malignant and benign glands.

Our high-throughput system requires minimal human interaction. HNCut only requires a few reference colors selected from a region of interest on a single representative image. Our system is then able to automatically segment and classify the target objects on the remaining images in the dataset without the need for further human interaction. While in this work our system is evaluated in the context of segmentation and classification of glands on prostate histopathology images, the system could be applied to a wide domain of problems where precise quantification of morphological traits is critical, such as breast lesion morphology on DCE-MRI [12].

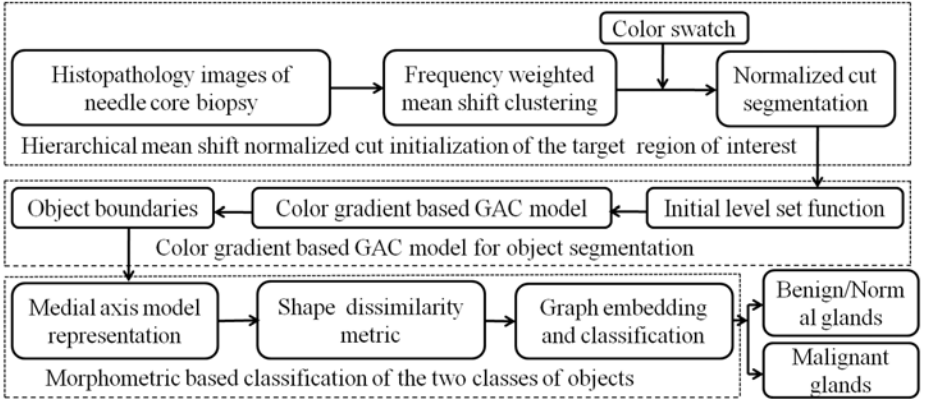


Fig. 1. Flowchart of our integrated detection, segmentation, and classification system

2 Gland Detection and Segmentation

2.1 Notation

The following notations will be used throughout the paper: $\mathcal{C} = (C, f)$ denotes the 2D image scene where $C \in \mathbb{R}^2$ is a grid of pixels $c \in C$. The pixels c are in a 2D Cartesian grid defined by $c = (x, y)$. The image intensity function $\mathbf{f}(c)$ assigns a three element intensity vector to pixel $c \in C$. The level set function is defined as $\phi(t, c)$. $\mathbb{C} = \{c \in \Omega : \phi(c) = 0\}$ is the zero level set. Ω denotes a bounded open set in \mathbb{R}^2 space. $\Omega_f = \{c \in \Omega : \phi(c) > 0\}$ denotes a foreground region while $\Omega_b = \{c \in \Omega : \phi(c) < 0\}$ denotes the background region. $\|\cdot\|$ denotes the L_2 normal in real space. $\delta(\phi)$ is the Delta function.

2.2 Hierarchical Mean Shift Based Normalized Cuts Detection Scheme

The hierarchical mean shift based normalized cuts (HNCut) scheme was originally presented in [9] for rapidly and accurately segmenting the object class of interest. By operating in the color domain, as opposed to the spatial domain (on pixels), the scheme is able to rapidly identify the gland regions even on very large images. The scheme is outlined below:

1. User selects the domain swatch defined as a set of pixels that are representative of the target class;
2. Frequency weighted mean-shift clustering is performed on a multi-resolution color pyramid;
3. Normalized cuts is used on the reduced color space created by the weighted mean-shift algorithm.

HNCut is robust to human intervention; the first step is only applied to a single representative image containing the target class. After the color swatch has been selected from the region of interest in the first image, the same swatch may be applied to all other images. The resulting target objects make for an excellent initialization of the active contour model that is subsequently applied.

2.3 Geodesic Active Contour Model

Energy functional. Assume the image plane $\Omega \in \mathbb{R}^2$ is partitioned into 2 non-overlapping regions by a zero level set function ϕ : the foreground Ω_f and background Ω_b . The optimal partition of the image plane Ω by a zero level set function ϕ can be obtained through minimizing the energy functional as follows,

$$\begin{aligned} E(\phi) &= \alpha E_1(\phi) + \beta E_2(\phi) + \gamma E_3(\phi), \\ &= \alpha \int_{\mathbb{C}} g(\mathbf{f}(c)) dc + \beta \int_{\Omega_f} g(\mathbf{f}(c)) dc + \gamma \int_{\Omega} \frac{1}{2} (\|\nabla \phi\| - 1)^2 dc, \end{aligned} \quad (1)$$

where $E_1(\phi)$ is the energy functional of a traditional GAC model. $E_2(\phi)$ is inspired by the balloon force proposed in [13]. An additional term $E_3(\phi)$ is added to the energy functional to remove the re-initialization phase which is required as a numerical remedy for maintaining stable curve evolution in traditional level set methods [14].

The color gradient. The edge-detector function in the traditional GAC model and the balloon force are based on the calculation of the gray scale gradient of the image [10]. In this paper, the edge-detector function is based on the color gradient which is defined as $g(\mathbf{f}(c)) = \frac{1}{1+s(\mathbf{f}(c))}$. $s(\mathbf{f}(c))$ is the local structure tensor based color gradient which is defined as $s(\mathbf{f}(c)) = \sqrt{\lambda_+ - \lambda_-}$ [15], where λ_+ and λ_- are the maximum and minimum eigenvalues of the local structure tensor of each pixel in the image. It locally sums the gradient contributions from each image channel representing the extreme rates of change in the direction of their corresponding eigenvectors. The methodology for computing the color gradient

described above can be applied to different vectorial color representations such as RGB, HSV, and Luv.

Curve evolution function of GAC model. Based on the theory of the calculus of variations, the curve evolution function can be derived from the level set framework by minimizing the energy functional (1). The function is defined by the following partial differential equation:

$$\begin{cases} \frac{\partial \phi}{\partial t} = \delta(\phi) \{ \alpha \mathbf{div} \left[g(\mathbf{f}(c)) \frac{\nabla \phi}{\|\nabla \phi\|} \right] - \beta g(\mathbf{f}(c)) \} - \gamma \left[\Delta \phi - \mathbf{div} \left(\frac{\nabla \phi}{\|\nabla \phi\|} \right) \right], \\ \phi(0, c) = \phi_0(c), \end{cases} \quad (2)$$

where α , β , and γ are positive constant parameters, and $\phi_0(c)$ is the initial evolution functional which is obtained from the HNCut detection results (see Section 2.2). $\mathbf{div}(\cdot)$ is the divergence operator. As the re-initialization phase has been removed, ϕ_0 is defined as piecewise linear function of regions:

$$\phi_0(c) = \begin{cases} -\pi, & c \in \Omega_b; \\ 0, & c \in \mathbb{C}; \\ \pi, & c \in \Omega_f, \end{cases}$$

where Ω_f , \mathbb{C} , and Ω_b in the context of the problem addressed in this paper are the luminal regions, the boundaries of the luminal regions and the other tissues, respectively. π is a positive constant.

3 Diffomorphic Based Shape Characterization and Classification

3.1 Medial Axis Shape Model

The medial axis shape model M is defined by a set of pixels $m \in \Omega_f$ along the medial axis of an object, and a set of corresponding surface vectors \mathbf{v}_1 , \mathbf{v}_2 on the contour \mathbb{C} . Here \mathbf{v}_1 , \mathbf{v}_2 are comprised by the nearest pixels on the contour \mathbb{C} to the medial axis pixel m [16]. For a given object, we can define a distance

$$\text{map function } f^e(c) \text{ on the image space as, } f^e(c) = \begin{cases} 0 & c \in \mathbb{C}, \\ -\min_{p \in \mathbb{C}} \|c - p\| & c \in \Omega_f, \\ \min_{p \in \mathbb{C}} \|c - p\| & c \in \Omega_b. \end{cases}$$

Given this distance map, the medial axis is the local minimum along the gradient

map of the image, defined as $\hat{f}^e(c) = \left(\frac{\partial f^e(c)}{\partial x} \right)^2 + \left(\frac{\partial f^e(c)}{\partial y} \right)^2$. Atoms belonging

to the medial axis are obtained as $M = \{m : m \in C, \hat{f}^e(m) < \tau\}$. Empirically,

$\{\tau = 0.05 \left[\min_{c \in C} (\hat{f}^e(c)) \right]\}$ was found to give a well defined medial axis. $\forall m \in M$,

the two closest pixels on the contour \mathbb{C} can be defined as $\hat{p}_1 = \underset{p \in \mathbb{C}}{\operatorname{argmin}} \|m - p\|$,

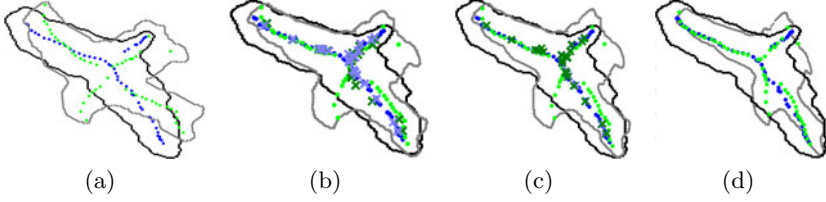


Fig. 2. (a) Two gland contours (black \mathbb{C}_a , gray \mathbb{C}_b) with corresponding medial atoms (blue M_a , green M_b) after initial affine alignment. Medial atoms for the fifth iteration with cluster centers of the shape models (light blue, dark green) for (b) initial cluster centers and (c) registration of cluster centers. Note cluster centers are aligned between the two gland contours after the registration. (d) The medial atoms of gland contours after final registration

and $\hat{p}_2 = \underset{p \in \mathbb{C}, p \neq \hat{p}_1}{\operatorname{argmin}} \|m - p\|$, and the corresponding surface vectors are defined $\mathbf{v}_1 = \hat{p}_1 - m$, and $\mathbf{v}_2 = \hat{p}_2 - m$.

3.2 Medial Axis Model Comparison

A dissimilarity metric is calculated between each pair of medial axis representations M_i and M_j , where $i, j \in \{1, \dots, N\}$. Here N refers to the number of glands. Briefly the steps of the comparison are:

1. M_i is registered to M_j using a point-based diffeomorphic registration algorithm originally presented in [17]. Fuzzy k -means clustering determines correspondences between the medial axis models. From these correspondences, a diffeomorphic transformation is calculated to register M_i into the coordinate space of M_j . This process is iteratively repeated until a stopping criteria is met. Figure 2 shows an example of this registration technique displaying the initial alignment, a single clustering and registration step, and the final alignment.
2. Point correspondence between the medial atom sets $\tilde{m}_i^{\hat{u}} \in \tilde{M}_i$ and $m_j^{\hat{v}} \in M_j$ is found. We define \tilde{M}_i as the medial axis M_i registered to the medial axis model M_j . We determine point correspondence between two medial axes as, $(\hat{u}, \hat{v}) = \underset{\hat{u}, \hat{v}}{\operatorname{argmin}} \|\tilde{m}_i^{\hat{u}} - m_j^{\hat{v}}\|$.
3. From the point correspondences in Step 2, shape dissimilarity is calculated as

$$A_{ij} = \sum_{(\hat{u}, \hat{v})} \kappa_1 \|\tilde{m}_i^{\hat{u}} - m_j^{\hat{v}}\| + \kappa_2 \|\mathbf{v}_{i,1}^{\hat{u}} - \mathbf{v}_{j,1}^{\hat{v}}\| + \kappa_3 \|\mathbf{v}_{i,2}^{\hat{u}} - \mathbf{v}_{j,2}^{\hat{v}}\|. \quad (3)$$

where κ_1 , κ_2 , and $\kappa_3 > 0$ are selected so that $A_{ab} \geq 0$.

The medial axis model comparison is repeated over all objects $i, j \in \{1, \dots, N\}$, so that $A \in \mathbb{R}^{N \times N}$ is a high dimensional dissimilarity matrix.

3.3 Feature Extraction

From A , we define similarity matrix W , where $W_{ij} = e^{-A_{ij}/\sigma}$, and $\sigma > 0$ controls the width of the neighborhoods. D is diagonal matrix whose diagonal elements are defined as $d_{ii} = \sum_j W_{ij}$. Here A_{ij} and W_{ij} are elements of matrices A and W , respectively. From the Laplacian matrix $D - W$, we find a low dimensional space $\mathbf{Y} = (\mathbf{y}^{(1)}, \mathbf{y}^{(2)}, \dots, \mathbf{y}^{(N)})^T \in \mathbb{R}^{N \times d}$, where $N \gg d$, that attempts to preserve pairwise distances between glands in A . Let \mathbf{Y}^* be the set of all $N \times d$ matrices \mathbf{Y} such that $\mathbf{Y}^T D \mathbf{Y} = \mathbf{I}_d$. The DBS features of each gland will be determined from the optimal $\mathbf{Y} \in \mathbf{Y}^*$ by solving the following minimization problem [11]

$$\begin{aligned} \min_{\mathbf{Y} \in \mathbf{Y}^*} \quad & \sum_{i=1}^N \sum_{j=1}^N \|\mathbf{y}^{(i)} - \mathbf{y}^{(j)}\|^2 W_{ij} = \text{tr}(\mathbf{Y}^T (D - W) \mathbf{Y}), \\ \text{s.t} \quad & \mathbf{Y}^T D \mathbf{Y} = \mathbf{I}_d \end{aligned} \quad (4)$$

where $\mathbf{y}^{(i)} = (y_1(i), y_2(i), \dots, y_d(i))^T$ is the d -dimensional representation of the i -th gland and \mathbf{I}_d is the d -dimensional identity matrix. Each row vector in \mathbf{Y} is used to determine d -dimensional DBS features of a corresponding gland, where $d = 3$ in this work.

4 Experimental Design and Performance Measures

4.1 Data Description

The data set includes digitized images of whole-slide prostate needle core biopsy specimens obtained from 23 patients and stained with Hematoxylin & Eosin (H&E). All studies were obtained from the Hospital at the University of Pennsylvania (UPENN). Each sample was digitized at 20x optical magnification using an Aperio whole-slide digital scanner. For all images, an expert pathologist manually annotated regions of interest (ROI) with different class labels: benign epithelium, benign stroma, and Gleason grades 3 and 4. Within each ROI, a human observer manually segmented the lumen layer of each gland. A total of 105 ROIs were identified consisting of benign (23 ROIs, 66 glands), Gleason grade 3 (71 ROIs, 656 glands), and grade 4 (11 ROIs, 36 glands).

4.2 Quantitative Evaluation of Segmentation

Owing to the great deal of manual labor involved in segmenting the gland boundaries, we limited the quantitative evaluation to only glands present within 10 ROIs from 10 whole-slide images randomly selected. The boundaries of automated segmentation are defined as the contours of the zero level set function of active contour models after convergence. We evaluate the segmentation results via two types of measurements. For boundary-based measurements, mean absolute distance (MAD) was calculated as $\text{MAD} = \frac{1}{s} \sum_{\nu=1}^s \{\min_{\chi} \|c_{\nu} - c_{\chi}\|\}$, $\forall c_{\chi} \in \mathcal{G}$, $\forall c_{\nu} \in \mathcal{S}$

where $\mathcal{G} = \{c_\chi | \chi \in \{1, \dots, t\}\}$ and $\mathcal{S} = \{c_\nu | \nu \in \{1, \dots, s\}\}$ are closed boundaries of manual and automated segmentation, respectively. t and s represent the number of pixels on the boundaries of manual and automated segmentation, respectively. For region-based measurements we calculated overlap (OL), sensitivity (SN), specificity (SP), and positive predictive value (PPV). For each image, the set of pixels lying within the manual delineations of the glands is denoted as $\mathcal{A}(G)$. $\mathcal{A}(S)$ is the set of pixels whose level set functions are positive, after the convergence of active contour model. OL, SN, SP, and PPV are then defined as $OL = \frac{|\mathcal{A}(S) \cap \mathcal{A}(G)|}{|\mathcal{A}(S) \cup \mathcal{A}(G)|}$, $SN = \frac{|\mathcal{A}(S) \cap \mathcal{A}(G)|}{|\mathcal{A}(G)|}$, $SP = \frac{|C - \mathcal{A}(S) \cup \mathcal{A}(G)|}{|C - \mathcal{A}(G)|}$, and $PPV = \frac{|\mathcal{A}(S) \cap \mathcal{A}(G)|}{|\mathcal{A}(S)|}$, where $|\mathcal{S}|$ represents the cardinality of set \mathcal{S} .

4.3 Morphological Feature Set Evaluation

A support vector machine (SVM) classifier [18] was used to evaluate the discriminability of the DBS features, with higher SVM accuracy reflecting a feature set that is better able to describe morphometric differences between gland classes. In this experiment we (a) compare the performance of the DBS features versus traditional boundary based attributes (area, perimeter, area overlap ratio, average radial distance ratio, standard deviation of the normalized distance ratio, compactness, and smoothness [12]) and (b) evaluate whether, from a gland classification perspective, the results obtained from automated and manual segmentation were significantly different. Four feature sets were tested comprising of DBS or traditional morphological features from either automated or manual gland segmentations.

For all feature sets malignant glands were defined as all glands contained within ROIs of a Gleason grade 3 or 4, while benign glands are obtained from benign ROIs. The SVM classifier accuracy was evaluated by utilizing a leave-one-study-out approach. The leave-one-study-out approach selected a testing set consisting of all glands from one patient study while the training set was comprised of glands from the remaining 22 patient studies. We evaluated the accuracy of our automated segmentation by performing a paired t-test over all 23 test sets between automated and manual segmentation for each feature set. We hypothesize that if no significant difference is found between the classification accuracies of the manual and automated schemes, the automated segmentation results are as good as the manual segmentation.

5 Experimental Results and Discussion

5.1 Segmentation Evaluation

Table 1 shows the results of quantitative evaluation of segmentation by our automated GAC scheme in terms of MAD, OL, SN, SP and PPV across 10 ROIs from

Table 1. Quantitative evaluation of segmentation results for the system. The average and standard deviation of the MAD, OL, SN, SP and PPV over 40 glands and 10 ROI's have been reported

MAD	Overlap (OL)	Sensitivity (<i>SN</i>)	Specificity (<i>SP</i>)	PPV
2.06 \pm 0.2	0.62 \pm 0.07	0.85 \pm 0.01	0.94 \pm 0.003	0.68 \pm 0.08

Table 2. SVM classification accuracy evaluated for manual and automated segmentation as well as DBS or common morphological features sets for a leave-one-patient-out evaluation. Accuracy was calculated for 23 different testing sets. The *p*-values reported test the hypothesis that the underlying distributions are statistically dissimilar. In both cases the null hypothesis, the distribution are statistically similar, was accepted

Morphological Feature	Segmentation	Accuracy- Annotated Regions	P-Value
Common	Manual	79.47 \pm 4.71%	0.989
	Automated	81.30 \pm 10.14%	
DBS	Manual	82.89 \pm 3.97%	0.9596
	Automated	82.50 \pm 9.10%	

10 patient studies. The mean and standard deviation values in Table 1 show that our HNCut based GAC scheme is able to segment the lumen regions accurately.

5.2 DBS Feature Evaluation

Table 2 shows that for both morphological feature types, the source of the gland boundaries (manual or automated) did not affect the SVM's ability to classify glands. For both features sets, *p*-values are not statistically significant ($p < 0.05$), so we accept the null hypothesis that the classifier accuracy using features derived from the manual and automated segmentation are similar. DBS yields higher classifier accuracy compared to traditional morphological features, although this difference is not statistically significant.

Qualitative results are illustrated in Figure 3 (a). Three regions have been shown in Figures 3 (b), (c) and (d), respectively. From the magnified regions, one can see that the lumen regions have been correctly segmented. The corresponding explicit medial axis shape models of segmented glands, consisting of pixels belonging to the medial axis (light blue) and surface vectors (dark blue), are shown in Figures 3 (e), (f) and (g), respectively. Figure 4 illustrates the classification results obtained from module 3. In Figure 4(a), the region annotated by the blue line is the malignant portion of the slide as determined by the expert pathologist. Gland boundaries are displayed for glands labeled benign (black) and malignant (green). From Figure 4(a), we can see that most of the segmented glands are correctly classified, with most of the errors occurring at the borders.

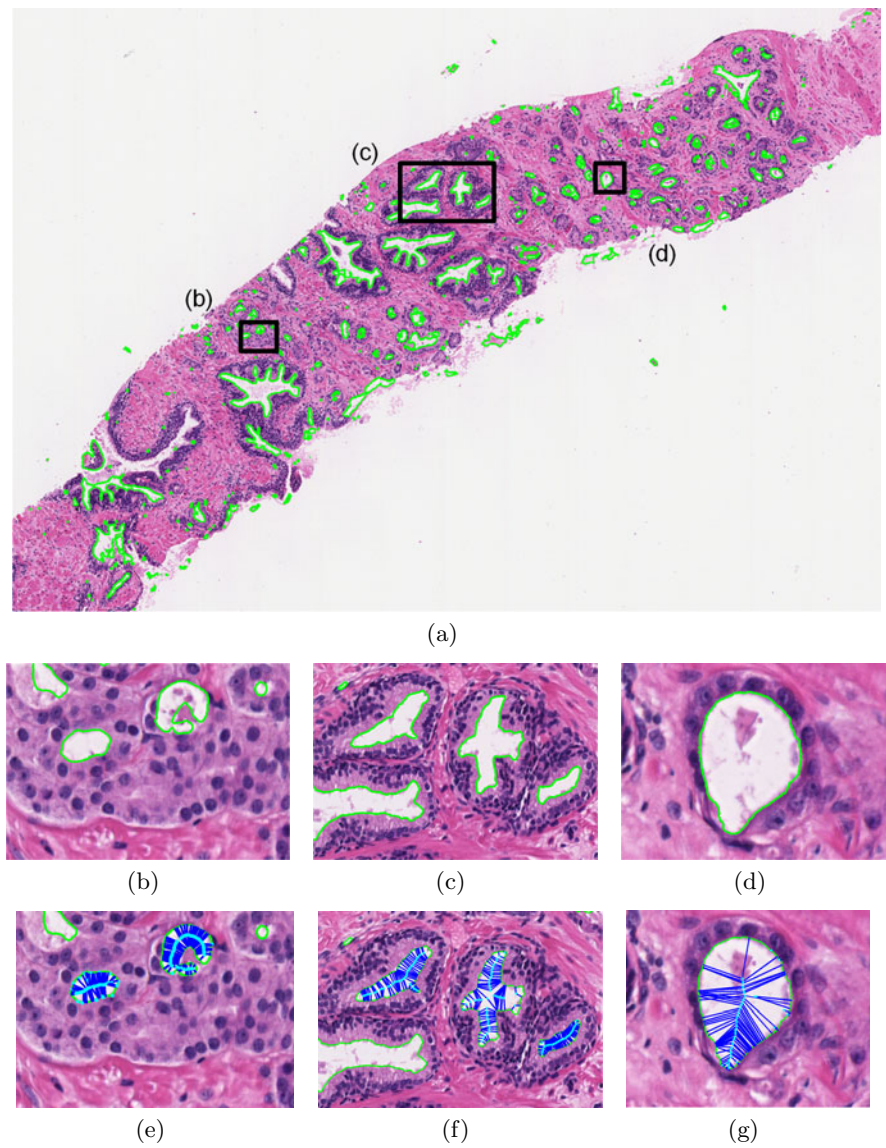


Fig. 3. (a) A representative example of the gland segmentation results (boundaries in green) from a whole-slide needle core biopsy. (b), (c), and (d) are three different ROIs from (a) which have been magnified to show gland details. The corresponding explicit medial axis shape model, consisting of the medial axis (light blue) and surface vectors (dark blue) are shown in (e), (f) and (g), respectively

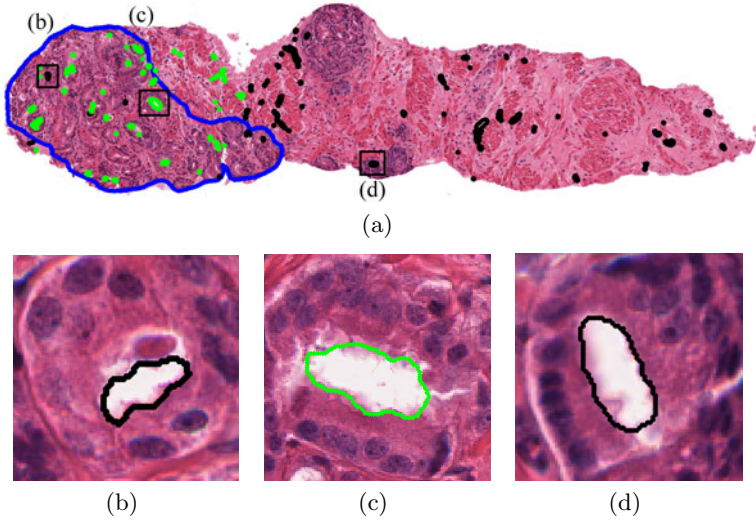


Fig. 4. (a) An example of whole-slide needle core biopsy of the prostate with malignant region delineated in blue. Glands labeled as benign/normal (black) and malignant (green) by the DBS SVM classifier are displayed. (b) An example of a malignant gland mislabeled by the DBS base classifier as benign. (c) A correctly labeled malignant and (d) benign gland by the DBS SVM classifier

6 Concluding Remarks

In this paper, we presented a high-throughput system for rapid and accurate gland detection, segmentation, and classification on high resolution digitized images of needle core biopsy samples of the prostate. The system is comprised of three modules: 1) a hierarchical mean shift normalized cut (HNCut) for initial gland detection, 2) a color gradient based geodesic active contour (GAC) model initialized via the result of HNCut, and the use of 3) a diffeomorphic based similarity (DBS) features to classify glands as benign or cancerous. The system requires minimal human interaction. The effectiveness of the automated segmentation of glands and the DBS features to distinguish cancerous and benign glands were evaluated and compared against corresponding manual segmentation obtained from 23 H & E stained prostate studies. Classification accuracy in distinguishing benign from malignant glands when using the automated segmentation scheme was $82.5 \pm 9.10\%$, while the corresponding accuracy with manual segmentation was $82.89 \pm 3.97\%$; no statistically significant differences were identified between the two segmentation schemes.

References

1. Madabhushi, A.: Digital pathology image analysis: opportunities and challenges. *Imaging in Medicine* 1(1), 7–10 (2009)
2. Gleason, D.F.: Histologic grading of prostate cancer: A perspective. *Human Pathology* 23(3), 273–279 (1992); *The Pathobiology of Prostate Cancer-Part 1*

3. Doyle, S., Feldman, M., Tomaszewski, J., Madabhushi, A.: A boosted bayesian multi-resolution classifier for prostate cancer detection from digitized needle biopsies. *IEEE Transactions on Biomedical Engineering* (in Press)
4. Monaco, J.P., Tomaszewski, J.E., Feldman, M.D., Hagemann, I., Moradi, M., Mousavi, P., Boag, A., Davidson, C., Abolmaesumi, P., Madabhushi, A.: High-throughput detection of prostate cancer in histological sections using probabilistic pairwise markov models. *Medical Image Analysis* 14, 617–629 (2010)
5. Farjam, R., Soltanian-Zadeh, H., Jafari-Khouzani, K., Zoroofi, R.: An image analysis approach for automatic malignancy determination of prostate pathological images. *Cytometry Part B (Clinical Cytometry)* 72(B), 227–240 (2007)
6. Tabesh, A., Teverovskiy, M., Ho-Yuen, P., Kumar, V.P., Verbel, D., Kotsianti, A., Saidi, O.: Multifeature prostate cancer diagnosis and gleason grading of histological images. *IEEE Transactions on Medical Imaging* 26(10), 1366–1378 (2007)
7. Sparks, R., Madabhushi, A.: Novel morphometric based classification via diffeomorphic based shape representation using manifold learning. In: *MICCAI 2010* (2010) (in press)
8. Paragios, N., Deriche, R.: Geodesic active regions and level set methods for supervised texture segmentation. *International Journal of Computer Vision* 46(3), 223–247 (2002)
9. Janowczyk, A., Chandran, S., Singh, R., Sasaroli, D., Coukos, G., Feldman, M.D., Madabhushi, A.: Hierarchical normalized cuts: Unsupervised segmentation of vascular biomarkers from ovarian cancer tissue microarrays. In: Yang, G.-Z., Hawkes, D., Rueckert, D., Noble, A., Taylor, C. (eds.) *MICCAI 2009*. LNCS, vol. 5761, pp. 230–238. Springer, Heidelberg (2009)
10. Caselles, V., Kimmel, R., Sapiro, G.: Geodesic active contours. *International Journal of Computer Vision* 22(1), 61–79 (1997)
11. Belkin, M., Niyogi, P.: Laplacian eigenmaps for dimensionality reduction and data representation. *Neural Computation* 15(6), 1373–1396 (2003)
12. Agner, S., Soman, S., Libfeld, E., McDonald, M., Thomas, K., Englander, S., Rosen, M., Chin, D., Noshier, J., Madabhushi, A.: Textural kinetics: A novel dynamic contrast enhanced (DCE)- MRI feature for breast lesion classification. *Journal of Digital Imaging* (in press)
13. Cohen, L.D.: On active contour models and balloons. *CVGIP: Image Underst.* 53(2), 211–218 (1991)
14. Li, C., Xu, C., Gui, C., Fox, M.D.: Level set evolution without re-initialization: A new variational formulation. In: *CVPR*, vol. 1, pp. 430–436 (2005)
15. Sapiro, G.: Color snakes. *Computer Vision and Image Understanding* 68(2), 247–253 (1997)
16. Blum, H.: A transformation for extracting new descriptors of shape. In: *Models for the Perception of Speech and Visual Form*, pp. 367–380. MIT Press, Cambridge (1967)
17. Guo, H., Rangarajan, A., Joshi, S.: Diffeomorphic point matching. In: *Handbook of Mathematical Models in Computer Vision*, pp. 205–219. Springer, US (2005)
18. Cortes, C., Vapnik, V.: Support-vector networks. *Machine Learning* 20, 273–297 (1995)